Dalton Transactions

ROYAL SOCIETY OF CHEMISTRY

PAPER

View Article Online
View Journal | View Issue

Cite this: *Dalton Trans.*, 2023, **52**, 13565

Peripheral site modification in a family of dinuclear $[Dy_2(hynad)_{2-6}(NO_3)_{0-6}(sol)_{0-2}]^{0/2-}$ single-molecule magnets bearing a $\{Dy_2(\mu\text{-}OR)_2\}^{4+}$ diamond-shaped core and exhibiting dissimilar magnetic dynamics†

Alexandros S. Armenis,[a] Dimitris I. Alexandropoulos,[b] Anne Worrell,[c] Luís Cunha-Silva,[d] Kim R. Dunbar[b] and Theocharis C. Stamatatos *[a,e]

The first use of the organic chelate *N*-hydroxy-1,8-naphthalimide (hynadH) in Dy^{III} chemistry has unveiled access to a synthetic 'playground' composed of four new dinuclear complexes, all of which possess the same planar $\{Dy_2(\mu\text{-}OR)_2\}^{4+}$ diamond-shaped core, resulting from the bridging and chelating capacity of the hynad$^-$ groups. The structural stability of the central $\{Dy_2\}$ core has allowed for the modulation of the peripheral coordination sites of the metal ions, and specifically the NO_3^-/hynad$^-$ ratio of capping groups, thus affording the compounds $[Dy_2(hynad)_2(NO_3)_4(DMF)_2]$ (**1**), $(Me_4N)_2[Dy_2(hynad)_2(NO_3)_6]$ (**2**), $[Dy_2(hynad)_4(NO_3)_2(H_2O)_2]$ (**3**), and $[Dy_2(hynad)_6(H_2O)_2]$ (**4**). Because of the chemical and structural modifications in the series **1–4**, the Dy^{III} coordination polyhedra are also dissimilar, comprising the muffin (**1** and **3**), tetradecahedral (**2**), and spherical tricapped trigonal prismatic (**4**) geometries. Complexes **1**, **2**, and **4** exhibit a ferromagnetic response at low temperatures, while **3** is antiferromagnetically coupled. All compounds exhibit out-of-phase (χ''_M) ac signals as a function of ac frequency and temperature, thus behaving as single-molecule magnets (SMMs), in the absence or presence of applied dc fields. Interestingly, the hynad$^-$-rich and nitrato-free complex **4**, demonstrates the largest energy barrier (U_{eff} = 69.62(1) K) for the magnetization reversal which is attributed to the presence of the two axial triangular faces of the spherical tricapped trigonal prism by the negatively charged O-atoms of the hynad$^-$ ligands.

Received 9th August 2023,
Accepted 11th September 2023

DOI: 10.1039/d3dt02596a

rsc.li/dalton

1. Introduction

A new era of single-molecule magnets (SMMs) has unfolded since the discovery of mononuclear[1] and polynuclear[2] 4f-metal complexes with fascinating properties that are significantly different from those previously documented in 3d-metal complexes.[3] SMMs are discrete molecular compounds that exhibit slow magnetization relaxation at the molecular level and hysteresis loops due to the existence of an energy barrier for the magnetization reversal.[4] SMMs have been proposed as potential candidates for technological applications, such as information storage,[5] molecular spintronics,[6] quantum computation,[7] and magnetic refrigeration.[8]

A key 'player' in the field of 4f metal-based SMMs is the Dy^{III} ion, due to the large magnetic anisotropy which arises from strong spin–orbit coupling, as well as the bistable ground state resulting from the odd number of electrons ($4f^9$) according to Kramers theorem.[9] Consequently, the Dy^{III} ion has played a pivotal role in the pursuit of efficient SMMs with large energy barriers (U_{eff}) for the magnetization reversal and high blocking temperatures (T_B).[10] The enhancement of the magnetic anisotropy for an oblate-shaped ion, such as Dy^{III}, can be achieved by either chemical or structural means, such as placing strong axial ligand fields with weak ligand fields in the equatorial plane,[11] or preparing highly symmetric com-

[a]*Department of Chemistry, University of Patras, 26504 Patras, Greece. E-mail: thstama@upatras.gr, alexarmenis1996@gmail.com; Tel: +30 2610 996730*
[b]*Department of Chemistry, Texas A&M University, College Station, Texas 77843, USA. E-mail: dalexandrop4@gmail.com, dunbar@chem.tamu.edu*
[c]*Department of Chemistry, 1812 Sir Isaac Brock Way, Brock University, L2S 3A1 St Catharines, Ontario, Canada. E-mail: aw12vt@brocku.ca*
[d]*LAQV/REQUIMTE & Department of Chemistry and Biochemistry, Faculty of Sciences, University of Porto, 4169-007 Porto, Portugal. E-mail: l.cunha.silva@fc.up.pt*
[e]*Institute of Chemical Engineering Sciences, Foundation for Research and Technology – Hellas (FORTH/ICE – HT), Platani, P.O. Box 1414, 26504 Patras, Greece*

†Electronic supplementary information (ESI) available: Crystal data and refinement parameters, structural data (tables and figures), and additional magnetism figures and tables for complexes **1–4**. CCDC 2278244 (**1**), 2278245 (**2**), 2278246 (**3**) and 2278247 (**4**). For ESI and crystallographic data in CIF or other electronic format see DOI: **https://doi.org/10.1039/d3dt02596a**

plexes with ideal lanthanide coordination geometries (*i.e.*, D_{4d}, D_{5h}, and D_{6h}).[12] Maximizing the magnetic anisotropy results in large energy splitting of the m_J microstates of the ground state ($^6H_{15/2}$) and subsequently large U_{eff} values (exceeding 2000 K), high blocking temperatures (up to 80 K), and dominant thermally activated relaxation mechanisms (Orbach process) observed in a number of mononuclear organometallic Dy^{III} complexes.[13] However, there are some under-barrier demagnetization pathways, such as the Raman process, which are favored due to the perturbation of the relaxing spins from the lattice thermal energy (phonons) which are detrimental to the retention of the magnetization.[14] Another major undesired mechanism is Quantum Tunneling of Magnetization (QTM) in which the spin tunnels through the barrier without following the thermally activated, stepwise Orbach process and is typically operative at low temperatures. The tunneling process is observed as a step in the hysteresis loops of magnetization (M) *vs.* field (H) plots due to the loss of magnetization near zero field and is a common feature in most non-organometallic, high-performance Dy^{III} SMMs.[14,15]

One of the main synthetic strategies to circumvent under barrier relaxation processes is the preparation of radical-bridged dinuclear lanthanide (Ln) complexes, such as the family of [Ln^{3+}–N_2^{3-}–Ln^{3+}] complexes,[16a] in which radical anionic ligands penetrate the inner 4f orbitals which leads to strong magnetic coupling between the 4f-metal ions.[16] Furthermore, metal–metal bonding between Ln ions has shown considerable promise, for example the mixed-valence dinuclear complex [$(Cp^{iPr5})_2Ln_2I_3$], where Cp^{iPr5} is the pentaisopropylcyclopentadienyl anion and Ln = Gd, Tb, or Dy.[17] The metal ions in this family of metal–metal bonded systems exhibit a Ln–Ln bond by sharing a d electron in the $5d_{z^2}$ orbital, rendering this molecular system an ultrahard magnet with open hysteresis loops up to 80 K and coercivities comparable with those of commercial magnets (*i.e.*, $SmCo_5$ and $Nd_2Fe_{14}B$).

Among the polynuclear lanthanide complexes that have been investigated in the area of molecular magnetism, dinuclear complexes have been widely explored because they constitute the most simple platform to investigate magnetic exchange coupling between two spin-carriers.[2,18] The choice of chelating/bridging organic ligands is of paramount importance in such molecular systems, as they should mainly consist of O-donor atoms to satisfy the oxophilicity of Ln ions. In this regard, we recently targeted the ligand *N*-hydroxy-1,8-naphthalimide (hynadH; Scheme 1), which, upon deprotonation, can act as a pocket-like, C_2 symmetric ligand for bridging and chelating two Ln^{III} atoms.

Herein we report the syntheses, structures, and magnetic characterization of a new family of {Dy_2} complexes with a $\{Dy_2(hynad)_2\}^{4+}$ planar core comprising the four compounds [$Dy_2(hynad)_2(NO_3)_4(DMF)_2$] (**1**), [$(Me_4N)_2[Dy_2(hynad)_2(NO_3)_6$] (**2**), [$Dy_2(hynad)_4(NO_3)_2(H_2O)_2$] (**3**), and [$Dy_2(hynad)_6(H_2O)_2$] (**4**). The ferromagnetic *vs.* antiferromagnetic coupling for compounds **1**, **2**, and **4** *versus* **3**, respectively, has been attributed to their dissimilar metrical parameters, including the intramolecular Dy⋯Dy separations, the Dy–O core distances, and the ligand's configuration with respect to the {Dy_2O_2} core. Interestingly, all complexes exhibit slow relaxation of their magnetization and SMM properties in the presence or absence of an external magnetic field. The different magnetic dynamics of **1–4** have been rationalized by means of analyzing the Dy^{III} coordination polyhedra and the orientation of the axial magnetic anisotropy along the stronger Dy–O bonds.

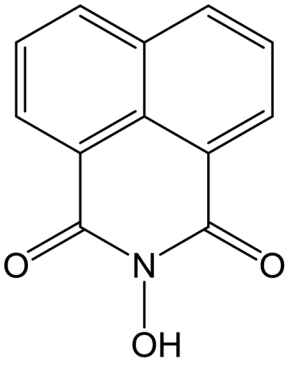

hynadH

Scheme 1 Structural formula and abbreviation of the ligand *N*-hydroxy-1,8-naphthalimide (hynadH) used in this study.

2. Experimental section

2.1. Synthesis

All reactions were performed under aerobic conditions using chemicals and solvents as received without further purification.

[$Dy_2(hynad)_2(NO_3)_4(DMF)_2$] (1). To a stirred, orange solution of hynadH (0.10 mmol, 0.021 g) and NEt_3 (0.10 mmol, 0.014 mL) in a solvent mixture of MeCN (10 mL) and DMF (10 mL) was added solid $Dy(NO)_3{\cdot}5H_2O$ (0.10 mmol, 0.044 g). The resulting yellow solution was stirred for 10 minutes and then filtered. The filtrate was left to slowly evaporate at room temperature and, after 4 days, X-ray quality yellow plate-like crystals of **1** were obtained. The crystals were collected by filtration, washed with cold MeCN (2 × 2 mL) and Et_2O (2 × 2 mL), and dried in air. The yield was 40% (based on Dy). The air-dried solid was analyzed as **1**. Anal. Calcd for $C_{30}H_{26}Dy_2O_{20}N_8$: C, 31.51; H, 2.29; N, 9.80. Found: C, 31.42; H, 2.17; N, 9.91. Selected IR data (ATR): ν = 2978 (w), 1645 (s), 1588 (m), 1481 (m), 1382 (m), 1293 (vs), 1082 (w), 1050 (m), 1025 (m), 908 (m), 844 (w), 771 (s), 683 (m), 564 (m), 463 (m).

[$(Me_4N)_2[Dy_2(hynad)_2(NO_3)_6]{\cdot}2MeCN$ (2·2MeCN). To a stirred, orange solution of hynadH (0.10 mmol, 0.021 g) and $Me_4NOH{\cdot}5H_2O$ (0.10 mmol, 0.018 g) in a solvent mixture of MeCN (10 mL) and DMF (10 mL) was added solid $Dy(NO)_3{\cdot}5H_2O$ (0.10 mmol, 0.044 g). The resulting yellow solution was stirred for 10 minutes and then filtered. The filtrate was left to slowly evaporate at room temperature and, after 7 days, X-ray quality

yellow plate-like crystals of **2**·2MeCN were obtained. The crystals were collected by filtration, washed with cold MeCN (2 × 2 mL) and Et_2O (2 × 2 mL), and dried in air. The yield was 45% (based on Dy). The air-dried solid was analyzed as **2**. Anal. Calcd for $C_{32}H_{36}Dy_2N_{10}O_{24}$: C, 30.27; H, 2.86; N, 11.03. Found: C, 30.41; H, 2.92; N, 2.69. Selected IR data (ATR): ν = 1648 (s), 1603 (m), 1586 (m), 1465 (s), 1302 (vs), 1252 (w), 1081 (w), 1034 (s), 948 (m), 909 (m), 847 (m), 775 (s), 705 (m), 550 (m), 530 (m), 463 (m).

$[Dy_2(hynad)_4(NO_3)_2(H_2O)_2]$·2DMF (3·2DMF). To a stirred, orange solution of hynadH (0.20 mmol, 0.042 g) and NEt_3 (0.20 mmol, 0.028 mL) in a solvent mixture of MeCN (10 mL) and DMF (10 mL) was added solid $Dy(NO)_3·5H_2O$ (0.10 mmol, 0.044 g). The resulting yellow solution was stirred for 10 minutes and then filtered. The filtrate was slowly diffused with Et_2O (20 mL), and, after 2 days, X-ray quality orange-yellow, plate-like crystals of **3**·2DMF were obtained. The crystals were collected by filtration, washed with cold DMF (2 × 2 mL) and Et_2O (2 × 5 mL), and dried in air. The yield was 60% (based on Dy). The air-dried solid was analyzed as **3**·2DMF. Anal. Calcd for $C_{54}H_{42}Dy_2O_{22}N_8$: C, 43.83; H, 2.86; N, 7.57. Found: C, 43.89; H, 2.95; N, 7.44. Selected IR data (ATR): ν = 2980 (w), 1628 (m), 1565 (vs), 1458 (w), 1382 (m), 1337 (m), 1292 (vs), 1257 (s), 1087 (w), 1038 (s), 897 (s), 844 (m), 772 (vs), 724 (m), 682 (m), 544 (m), 491 (m).

$[Dy_2(hynad)_6(H_2O)_2]$·2DMF (4·2DMF). To a stirred, orange solution of hynadH (0.30 mmol, 0.063 g) and NEt_3 (0.30 mmol, 0.042 mL) in a solvent mixture of MeCN (10 mL) and DMF (10 mL) was added solid $Dy(NO)_3·5H_2O$ (0.10 mmol, 0.044 g). The resulting dark red solution was stirred for 30 minutes and then filtered. The filtrate was left to slowly evaporate at room temperature, and, after 12 days, X-ray quality red plate-like crystals of **4**·2DMF were obtained. The crystals were collected by filtration, washed with cold DMF (2 × 2 mL) and Et_2O (2 × 5 mL), and dried in air. The yield was 50% (based on Dy). The air-dried solid was analyzed as **4**·2DMF. Anal. Calcd for $C_{78}H_{54}Dy_2O_{22}N_8$: C, 52.62; H, 3.06; N, 6.29. Found: C, 52.77; H, 3.21; N, 6.15. Selected IR data (ATR): ν = 3061 (w), 1658 (m), 1631 (m), 1575 (vs), 1414 (w), 1400 (m), 1264 (s), 1236 (s), 1079 (w), 1035 (s), 898 (s), 845 (m), 772 (vs), 545 (m), 482 (m).

2.2. X-Ray crystallography

Single-crystal X-ray diffraction data were collected on yellow and yellow-orange plate-like crystals of **1** (0.05 × 0.02 × 0.01 mm), **2**·2MeCN (0.08 × 0.05 × 0.05 mm), and **3**·2DMF (0.10 × 0.08 × 0.08 mm) using a Rigaku Oxford Diffraction XtaLAB Synergy diffractometer equipped with a HyPix-6000HE area detector at 173 K (for **1** and **2**) and 150 K (for **3**) utilizing Cu Kα (λ = 1.54184 Å) from PhotonJet micro-focus X-ray source. The structures were solved using the charge-flipping algorithm, as implemented in the program SUPERFLIP,[19] and refined by full-matrix least-squares techniques against F_o^2 using the SHELXL program[20] through the OLEX2 interface.[21] The non-hydrogen atoms were successfully refined using anisotropic displacement parameters, and hydrogen atoms bonded to the carbon of the ligands and those of the aqua groups were placed at their idealized positions using appropriate HFIX instructions in SHELXL. All atoms were included in subsequent refinement cycles in riding-motion approximation with isotropic thermal displacement parameters (U_{iso}) fixed at 1.2 or 1.5U_{eq} of the relative atom. A red plate-like single-crystal of **4**·2DMF (0.16 × 0.10 × 0.03 mm) was selected and mounted onto a cryoloop using inert oil.[22] Diffraction data were collected at 150 K on a Bruker X8 Kappa APEX II Charge-Coupled Device (CCD) area-detector diffractometer controlled by the APEX2 software package[23] (Mo Kα graphite-monochromated radiation, λ = 0.71073 Å), and equipped with an Oxford Cryosystems Series 700 cryostream monitored remotely with the software interface Cryopad.[24] Images were processed with the software SAINT,[25] and absorption effects corrected with the multi-scan method implemented in SADABS.[26] The structure was solved by direct methods employed in SHELXS-97,[27,28] allowing the immediate location of the metal ions. The other non-hydrogen atoms of the complex were located from difference Fourier maps calculated by successive full-matrix least-squares refinement cycles on F^2 using SHELXL-2013,[28,29] and refined with anisotropic displacement parameters.

Substantial electron density was found in the data of compounds **3** and **4** due to disordered solvent molecules occupying the interstices. Our efforts to properly locate, model and refine these residues were unsuccessful, and the investigation for the total potential solvent area using the software package PLATON clearly confirmed the existence of cavities with solvent accessible void volume. Consequently, the original data sets were treated with the program SQUEEZE,[30] a part of the PLATON package of crystallographic software, which calculates the contribution of the disordered electron density in the void spaces and adds this to the calculated structure factors from the structural model when refining against the . hkl file.

Figures of the structures were created using Diamond 3 and Mercury software packages.[31,32] Unit cell parameters, structure solution and refinement details for **1–4** are summarized in Table S1.† Further crystallographic details can be found in the corresponding CIF files provided in the ESI.†

2.3 Physical measurements

Infrared spectra were recorded in the solid state on a Bruker FT-IR spectrometer (ALPHA's Platinum ATR single reflection) in the 4000–400 cm^{-1} range. Elemental analyses (C, H, and N) were performed by the University of Patras microanalytical service. Variable-temperature direct and alternating current (dc and ac, respectively) magnetic susceptibility studies were performed at the University of Texas A&M at San Antonio (UTSA) Chemistry Department using a Quantum Design MPMS XL SQUID magnetometer with a temperature range of 1.9–300 K. Pascal's constants were used to estimate the diamagnetic correction, which was subtracted from the experimental susceptibility to give the molar paramagnetic susceptibility (χ_M).[33]

3. Results and discussion

3.1 Synthetic methods

To approach the targeted synthesis of dinuclear 4f-metal complexes, the choice of the organic bridging and chelating ligand is pivotal. To this end, the hynad$^-$ organic chelate provides specific chemical, steric and electronic features that render it an ideal ligand to facilitate the synthesis of $\{Dy_2\}$ complexes. Hynad$^-$ belongs to the family of *N*-substituted naphthalene imides and possesses two carbonyls (C=O) and an alkoxido type (R_2N-O^-) group which can simultaneously form two five-membered chelating rings with two Dy^{III} atoms and act as a monoatomic bridge to support the formation of a $\{Dy_2(\mu\text{-}OR)_2\}$ core. The lanthanide oxophilicity is satisfied by the O-donor atoms of hynad$^-$ whereas the naphthalene substituent of the ligand's backbone provides rigidity and an overall planarity of the targeted $\{Dy_2(hynad)_2\}^{4+}$ unit. Interestingly, the ligand hynadH, either in its neutral or deprotonated forms, has only been previously employed in 3d-metal chemistry for the synthesis of a tetranuclear Mn^{II} cluster, and di- and mononuclear Co^{II} complexes; none of these compounds exhibited SMM behavior.[34] Thus, we decided to use hynadH as a bridging/chelating ligand in Dy^{III} chemistry as a means of obtaining dinuclear complexes with SMM behavior, but we were surprised to discover that the chemistry produced $\{Dy_2\}$ compounds (**1–4**) with the same core structure but with different peripheral ligation and dissimilar SMM dynamics.

The first reaction that was performed was the 1 : 1 : 1 reaction between $Dy(NO_3)_3{\cdot}5H_2O$, hynadH and NEt_3 in a solvent mixture of MeCN/DMF (1 : 1, v/v) to increase the solubility of the reactants and the final product. The yellow crystalline compound was revealed to be the dinuclear complex $[Dy_2(hynad)_2(NO_3)_4(DMF)_2]$ (**1**) bearing a double alkoxido-bridged $\{Dy_2(\mu\text{-}OR)_2\}$ core supported by peripheral nitrato groups and DMF solvate molecules (*vide infra*). A subsequent systematic study was conducted,[35] firstly by replacing NEt_3 with the stronger base Me_4NOH without altering other synthetic parameters. After a week, yellow crystals of the anionic dinuclear complex $(Me_4N)_2[Dy_2(hynad)_2(NO_3)_6]{\cdot}2MeCN$ (**2**·2MeCN) were formed, revealing the first peripheral site modulation of the $\{Dy_2(\mu\text{-}OR)_2\}$ core from the set of hynad^{2-} *vs.* NO_3^- ligands (1 : 2 ratio in **1** *vs.* 1 : 3 ratio in **2**). Additional changes to the nature and strength of the external base did not yield any crystalline material but only oily products or amorphous precipitates.

The next synthetic step was to exert a chelate stress on the initial reaction which led to compound **1** by increasing the quantity of the hynadH ligand with respect to that of available nitrates, thus further manipulating the ratio of the two coordinating groups without affecting the dinuclear core structure. Indeed, the 1 : 2 : 2 reaction between $Dy(NO)_3{\cdot}5H_2O$, hynadH and NEt_3, in the same solvent mixture of MeCN/DMF (1 : 1, v/v), yielded orange-yellow crystals of the $[Dy_2(hynad)_4(NO_3)_2(H_2O)_2]{\cdot}2DMF$ (**3**·2DMF) compound featuring the same $\{Dy_2(\mu\text{-}OR)_2\}$ core albeit in a new hynad^{2-} *vs.* NO_3^- ligand ratio of 2 : 1. A further increase in the amount of chelate ligand by using a 1 : 3 : 3 reaction of $Dy(NO)_3{\cdot}5H_2O$, hynadH and NEt_3 in MeCN/DMF (1 : 1, v/v) yielded a red colored solution and single-crystals of $[Dy_2(hynad)_6(H_2O)_2]{\cdot}2DMF$ (**4**·2DMF), the fourth member of this family of diamond-shaped $\{Dy_2\}$ complexes and the first containing exclusively hynad^{2-} bound ligands. Although it would not have been possible to predict the formation of complex **4**, given the steric bulk of the chelate it is evident that the planarity of the central $\{Dy_2(hynad)_2\}^{4+}$ subunit provides the available space for its formation.

3.2. Description of structures

Selected interatomic distances and angles for **1–4** are listed in Tables S2–S5,† respectively. For the sake of brevity, only important metrical parameters will be discussed in the main text. Complexes **1–4** crystallize in the triclinic space group $P\bar{1}$, and they are centrosymmetric possessing an inversion center at the midpoint of the Dy1···Dy1′ distance. The compounds $(Me_4N)_2[Dy_2(hynad)_2(NO_3)_6]$ (**2**), $[Dy_2(hynad)_4(NO_3)_2(H_2O)_2]$ (**3**) and $[Dy_2(hynad)_6(H_2O)_2]$ (**4**) crystallize with two MeCN (**2**) and two DMF (**3**/**4**) solvate molecules, while compound $[Dy_2(hynad)_2(NO_3)_4(DMF)_2]$ (**1**) is crystal lattice solvate-free. The interstitial solvents in **2–4** weakly interact with the coordinated ligands, thus contributing to the intermolecular separations between the $\{Dy_2\}$ compounds.

For all four compounds **1–4** (Fig. 1–4), the two Dy^{III} atoms are doubly bridged by the deprotonated alkoxido-type O atom of two nearly planar, $\eta^1{:}\eta^2{:}\eta^1{:}\mu$ hynad$^-$ ligands, yielding a planar $\{Dy_2(\mu\text{-}OR)_2\}^{4+}$ diamond-shaped core (highlighted bonds in Fig. 1–4). The intra-dimer Dy1···Dy1′ distances are 4.018(4), 4.130(3), 4.094(3), and 4.133(5) Å, for **1–4**, respectively. In all cases, the central diamond-shaped core is completed by the two five-membered chelating rings from each hynad$^-$ ligand. In addition, for **1**, peripheral ligation is provided by two bidentate chelating NO_3^- groups and one terminally bound DMF molecules on each Dy^{III} atom. The NO_3^- groups are perpendicular to the nearly planar $\{Dy_2(\mu\text{-}hynad)_2\}^{4+}$ unit, while the coordinated DMF molecules are close to the axis that passes through the two Dy^{III} centers (Fig. S1a†). The displacement of the ligand's donor atoms O9 and O10 (and their symmetry-equivalent partners) out of the $\{Dy_2(\mu\text{-}O)_2\}$ best-mean-plane is 0.354 and 0.090 Å, respectively. The Dy1–O8–Dy1′ intra-dimer angle is 119.0(1)°. Each Dy^{III} atom in **1** is nine-coordinate, possessing a distorted "muffin-type" geometry (Fig. 1b), as confirmed by the continuous shape measures (CShM) approach of the SHAPE program[36] which allows one to numerically evaluate how much a particular polyhedron deviates from the ideal shape. The best fit was obtained for the muffin geometry (CShM value = 2.73 and Table S6†). Values of CShM larger than 3 correspond to a significant distortion from the ideal geometry.

In the case of $(Me_4N)_2[Dy_2(hynad)_2(NO_3)_6]$ (**2**), the coordinated DMF molecules have been replaced by two bidentate chelating NO_3^- groups (Fig. 2a), thus increasing the coordination number of each Dy^{III} atom from nine (in **1**) to ten. As a result, the coordination geometry of Dy^{III} atoms in **2** can be best described as tetradecahedral (Fig. 2b) with a CShM value

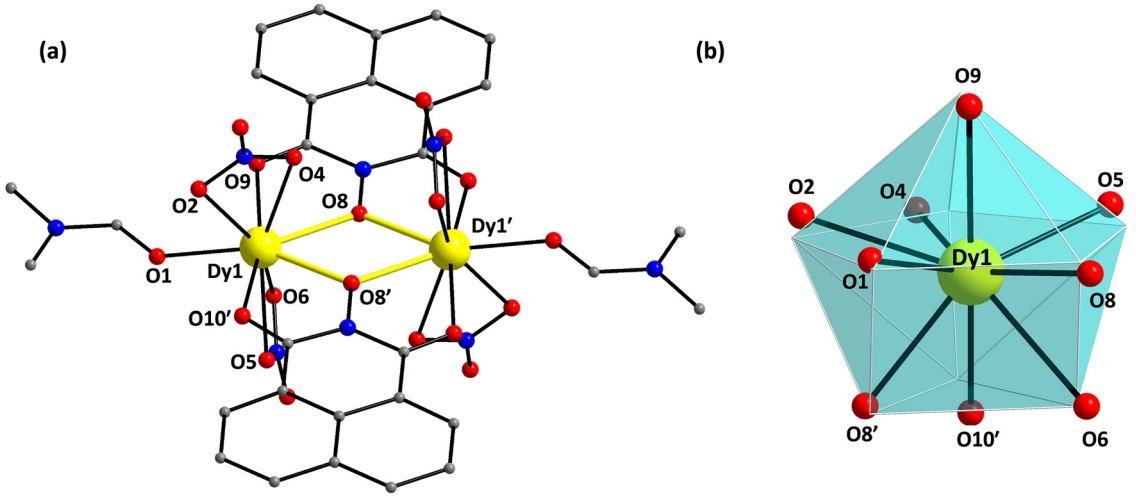

Fig. 1 (a) Partially labeled representation of the molecular structure of **1**, highlighting the $\{Dy_2(\mu\text{-}OR)_2\}^{4+}$ core with thick yellow bonds. (b) The muffin coordination polyhedron of the Dy^{III} centers in **1**. The smaller white spheres define the vertices of the corresponding ideal polyhedron. Color scheme: Dy^{III}, yellow; O, red; N, blue; C, grey. H-atoms are omitted for clarity. Symmetry code: (′) *–x*, *–y*, *–z*.

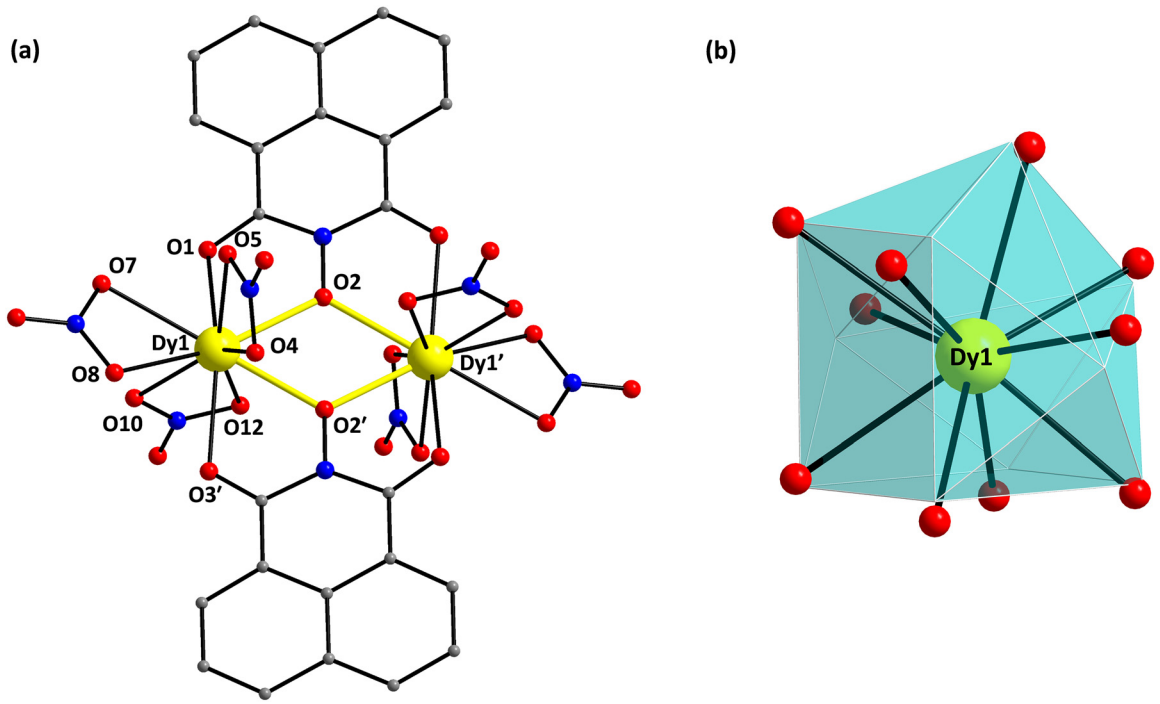

Fig. 2 (a) Partially labeled representation of the dinuclear cation in **2**, highlighting the $\{Dy_2(\mu\text{-}OR)_2\}^{4+}$ core with thick yellow bonds. (b) The tetradecahedron coordination polyhedron of the Dy^{III} centers in **2**. The smaller white spheres define the vertices of the corresponding ideal polyhedron. Color scheme: Dy^{III}, yellow; O, red; N, blue; C, grey. H-atoms are omitted for clarity. Symmetry code: (′) *–x*, *–y*, *–z*.

of 2.24 (Table S7†). The methyl groups of the Me_4N^+ cations are weakly interacting with the dangling O-atoms of the nitrato ligands, holding together the dianionic coordination compound. In **2**, the displacement of the ligand's donor atoms O1 and O3 (and their symmetry equivalents) out of the $\{Dy_2(\mu\text{-}O)_2\}$ best-mean-plane is 0.748 and 0.216 Å, respectively, thus imposing a significant twist on the ligand's backbone (Fig. S1b†), which is a noticeable difference in the structures of **1** and **2**. The Dy1–O2–Dy1′ intra-dimer angle is 121.2(1)°, very close to the value found in **1**. A comparison of the stereochemical features of **1** and **2** reveals a noteworthy feature which deserves discussion; the ligand hynad$^-$ (as defined by the best-mean-plane of all its atoms) in **2** is significantly tilted with respect to the planar $\{Dy_2O_2\}$ core by an angle of 13.0°, while the same

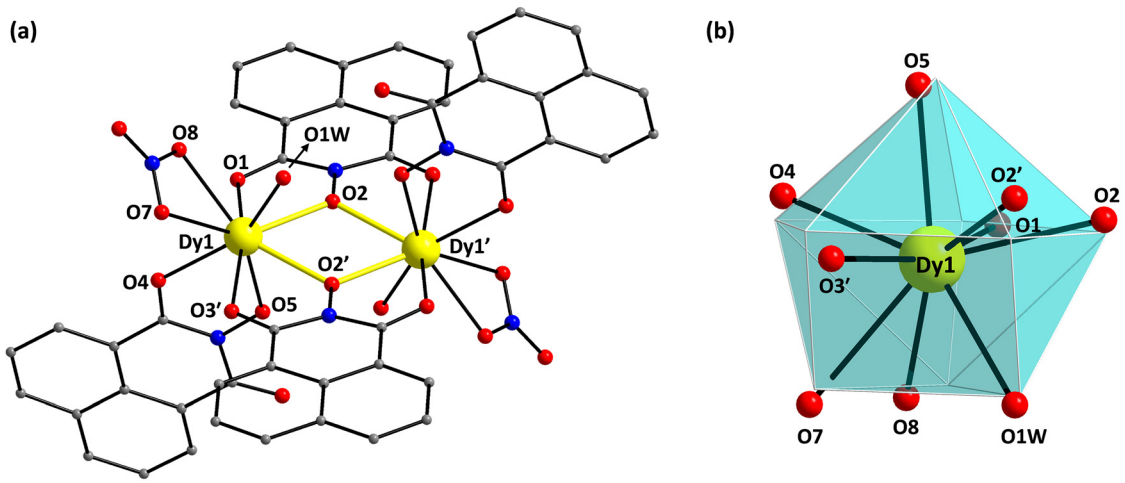

Fig. 3 (a) Partially labeled representation of the molecular structure of **3**, highlighting the $\{Dy_2(\mu\text{-}OR)_2\}^{4+}$ core with thick yellow bonds. (b) The muffin coordination polyhedron of the Dy^{III} centers in **3**. The smaller white spheres define the vertices of the corresponding ideal polyhedron. Color scheme: Dy^{III}, yellow; O, red; N, blue; C, grey. H-atoms are omitted for clarity. Symmetry code: (′) *–x*, *–y*, *–z*.

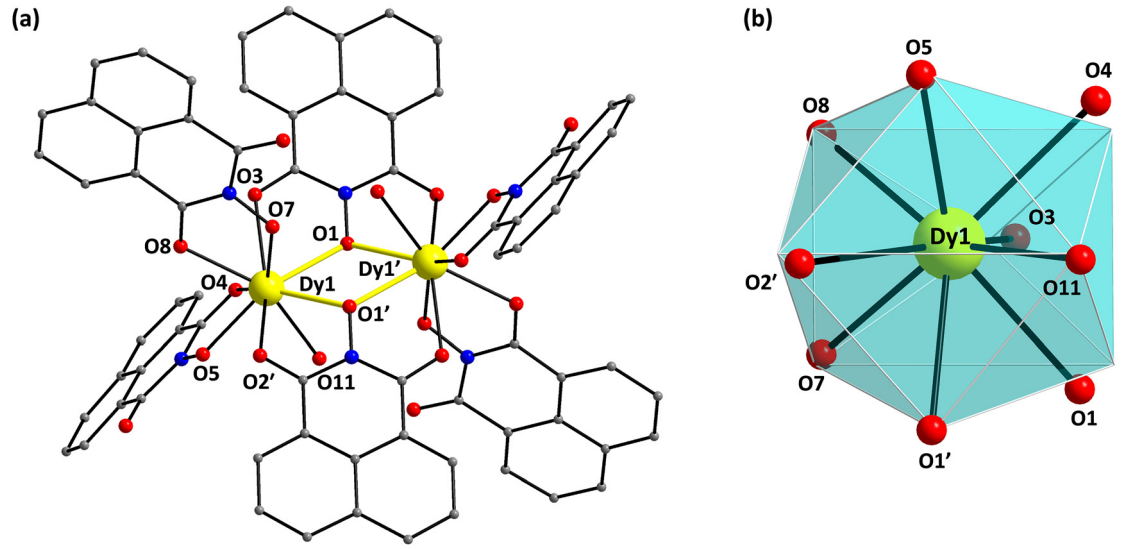

Fig. 4 (a) Partially labeled representation of the molecular structure of **4**, highlighting the $\{Dy_2(\mu\text{-}OR)_2\}^{4+}$ core with thick yellow bonds. (b) The spherical tricapped trigonal prismatic coordination polyhedron of the Dy^{III} centers in **4**. The smaller white spheres define the vertices of the corresponding ideal polyhedron. Color scheme: Dy^{III}, yellow; O, red; N, blue; C, grey. H-atoms are omitted for clarity. Symmetry code: (′) *–x*, *–y*, *–z*.

angle in **1** is only 5.4°. These features emphasize the flexible nature of hynad$^-$ upon coordination with the Dy^{III} centers.

In terms of intermolecular interactions, both **1** and **2** exhibit π–π stacking interactions with their neighboring counterparts through the naphthalene units of hynad$^-$ ligands (Fig. S2 and S3†). The centroid-to-centroid separations are 3.612 and 3.654 Å, while the shortest intermolecular Dy⋯Dy distance is 7.209 and 8.739 Å for **1** and **2**, respectively.

Complex $[Dy_2(hynad)_4(NO_3)_2(H_2O)_2]$ (**3**) is the first of its kind within the reported family of dinuclear compounds in that two hynad$^-$ groups occupy peripheral sites of the $\{Dy_2(hynad)_2\}^{4+}$ core, acting as $\eta^1{:}\eta^1$-bidentate chelating ligands (Fig. 3a) and each having an uncoordinated carbonyl O atom. Additional ligation is provided by two bidentate chelating NO_3^- groups and two terminal H_2O molecules, which complete the nine-coordinate geometry about each Dy^{III} atom. According to the SHAPE program, the best geometry that describes the Dy^{III} centers is that of a distorted muffin (CShM = 3.29; Fig. 3b and Table S6†). The Dy1–O2–Dy1′ intra-dimer angle is 117.9(2)°. The displacement of the core ligand's donor atoms O1 and O3 (and their symmetry-equivalent partners) out of the $\{Dy_2(\mu\text{-}O)_2\}$ best-mean-plane is 0.813 and 0.195 Å, respectively, while the ligand hynad$^-$ in whole forms an angle of 14.7° with respect to the $\{Dy_2O_2\}$ core. This leads to a more pronounced distortion of **3** as compared to the nitrato-rich **1** and **2** (Fig. S1c†).

Finally, the coordinated H_2O molecules (O1W and O1′W) form intramolecular H-bonds with the lattice DMF solvate molecules (O10 and O10′) and the deprotonated O-atoms of the bidentate chelating hynad$^-$ ligands (O5 and O5′); their dimensions are: O1W···O10 = 2.754(1) Å and O1W··· O5′ = 2.762(6) Å (Fig. S4†). Furthermore, the $\{Dy_2\}$ complexes in the crystal of **3**·2DMF interact intermolecularly with each other through π–π stacking interactions along the crystallographic *a*- and *c*-axes, thus creating an overall 2-D porous framework (Fig. S5 and S6†). The shortest intermolecular Dy···Dy distance in **3** is 10.885 Å.

The nitrato-free complex $[Dy_2(hynad)_6(H_2O)_2]$ (**4**) consists of two nine-coordinate Dy^{III} atoms (Fig. 4a), but, in this case, the metal centers adopt a spherical tricapped trigonal prismatic geometry as established by the SHAPE program (CShM = 2.05, Fig. 4b and Table S6†). Peripheral ligation about the $\{Dy_2(hynad)_2\}^{4+}$ core is provided by four additional $\eta^1{:}\eta^1$-bidentate chelating hynad$^-$ ligands (as in **3**) and two terminally-bound H_2O molecules. The Dy1–O1–Dy1′ intra-dimer angle is 117.6(2)°, essentially the same as that of **3**. The displacement of the core ligand's donor atoms O2 and O3 (and their symmetry-equivalent partners) out of the $\{Dy_2(\mu\text{-}O)_2\}$ best-mean-plane is 0.089 and 1.211 Å, respectively, which means that the O2/O2′ atoms are nearly co-parallel with the core subunit whereas the O3/O3′ atoms are distal from the core (Fig. S1d†). Interestingly, the bridging hynad$^-$ core ligands in **4** form an angle of 28.6° with respect to the $\{Dy_2O_2\}$ core, which is nearly twice the corresponding value found in **3**, thus imposing a significant twist on the structure; this is most likely due to the presence of the additional chelating hynad$^-$ groups at the peripheral sites of the compound.

Akin to **3**, the coordinated H_2O molecules (O11 and O11′) form intramolecular H-bonds with the interstitial DMF solvate molecules (O10 and O10′) and the deprotonated O-atoms of two bidentate chelating hynad$^-$ ligands (O7 and O7′); their dimensions are: O11···O10 = 2.780(1) Å and O11··· O7′ = 2.737 (6) Å. Moreover, the $\{Dy_2\}$ complexes in the crystal of **4**·2DMF are strongly interacting with each other through an extensive array of π–π stacking intermolecular interactions with centroid-to-centroid distances of 3.597 and 3.511 Å along the crystallographic *a*- and *c*-axes, respectively (Fig. S7 and S8†). The shortest intermolecular Dy···Dy distance in **4** is 11.013 Å, slightly larger than that of **3**.

3.3. Static magnetic properties

Direct current (dc) magnetic susceptibility studies were performed on analytically pure, microcrystalline samples of **1–4** in the 2–300 K temperature range under an applied magnetic field of 0.1 T (Fig. 5). The room temperature $\chi_M T$ values of 29.51 (**1**), 28.37 (**2**), 28.15 (**3**), and 28.27 (**4**) cm^3 mol^{-1} K are very close to the theoretical value of 28.34 cm^3 mol^{-1} K for two non-interacting Dy^{III} ions ($^6H_{15/2}$, S = 5/2, L = 5, g = 4/3). For complexes **1** and **2**, the $\chi_M T$ product remains almost constant until ~30–40 K, and then sharply increases reaching values of 45.63 and 45.49 cm^3 mol^{-1} K at 2 K, respectively, suggesting the presence of intramolecular ferromagnetic interactions

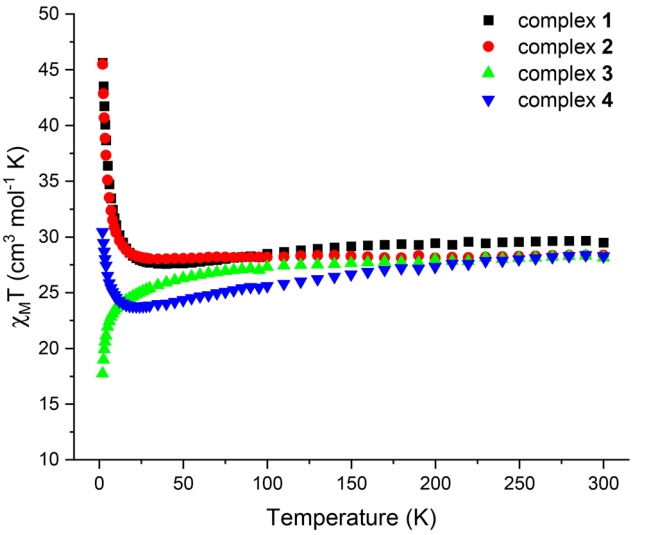

Fig. 5 Temperature dependence of the $\chi_M T$ product for complexes **1–4** recorded at a 0.1 T static dc field.

between the metal centers. In contrast to **1** and **2**, the $\chi_M T$ product of **3** decreases smoothly upon cooling until ~50 K and then more abruptly to a value of 17.76 cm^3 mol^{-1} K at 2 K. For complex **4**, the $\chi_M T$ product constantly decreases from 300 to ~30 K, followed by a small plateau between ~30 and 20 K, before increasing sharply to a value of 30.46 cm^3 mol^{-1} K at 2 K. The continuous decline of $\chi_M T$ as the temperature is lowered in **3** is primarily due to the depopulation of the crystal field m_J states of the ground state ($^6H_{15/2}$) in combination with the presence of weak intramolecular antiferromagnetic interactions between the Dy^{III} atoms, whereas the low-temperature increase of the $\chi_M T$ product for complex **4** is attributed to the onset of weak ferromagnetic interactions between the metal centers.

The field (H) dependence of the magnetization (M) for all complexes **1–4** at 2, 5, and 7 K are shown in Fig. S9–S12.† All of the compounds exhibit a relatively rapid increase at low fields without reaching saturation at the maximum applied field of 7 T, indicating the presence of magnetic anisotropy and/or low-lying excited states. The magnetization values at 7 T are 15.01 (**1**), 14.40 (**2**), 8.36 (**3**), and 16.34$N\mu_B$ (**4**), much lower than the expected saturation value (M_S) for two Dy^{III} ions ($M_S/N\mu_B = 20N\mu_B$); this is mainly attributed to the crystal field effects that induce strong magnetic anisotropy.

3.4. Dynamic magnetic properties

The following discussion is divided in such a manner as to compare the ac magnetic response of the reported compounds relative to one another. Therefore, to investigate the magnetization dynamics of complexes **1** and **2**, alternating current (ac) magnetic susceptibility measurements were performed at zero applied dc field in the temperature range of 1.8–20 K, under a weak ac field of 3.0 G, with frequencies ranging from 1–1000 Hz. As shown in Fig. 6, both complexes exhibit similar ac

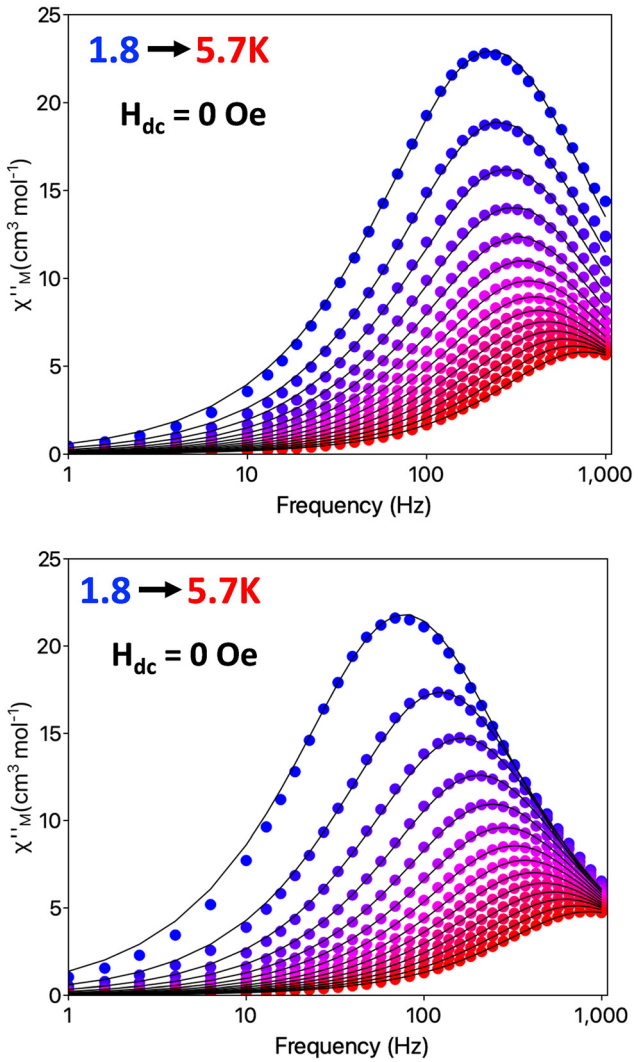

Fig. 6 Frequency-dependence of the out-of-phase (χ''_M) magnetic susceptibility data in zero dc field for **1** (top) and **2** (bottom), measured at 3.0 G ac field over the temperature range 1.8–5.7 K. Solid lines represent fits to the data, as described in the main text.

responses with frequency-dependent, out-of-phase (χ''_M) peaks of signals appearing below 5.7 K, thus suggesting the presence of slow relaxation of the magnetization consistent with SMM behavior.

To further examine the distribution of relaxation times (α), the Cole–Cole plots of both **1** and **2** were fit using a generalized Debye model (Fig. S13 and S14†).[37] The shapes of the plots deviate from the typical semicircular ones, yielding α values in the range of 0.16–0.03 (Tables S8 and S9†), indicative of a wide distribution of relaxation times which is consistent with the presence of multiple relaxation processes most likely due to a combination of thermally assisted and under-barrier relaxation mechanisms. Hence, to extract the temperature dependence of relaxation times (τ), and construct an Arrhenius-like plot, we fitted the data including Orbach, Raman, and QTM relaxation mechanisms to the overall magnetization behavior of complexes **1** and **2**, by using the following eqn (1):

$$\tau^{-1} = \tau_0^{-1} \exp(-U_{\text{eff}}/k_B T) + CT^n + \tau_{\text{QTM}}^{-1} \quad (1)$$

where τ^{-1} defines the relaxation rate, and the first term corresponds to the Orbach process in which τ_0 is the pre-exponential factor, $k_B T$ is the thermal energy, and U_{eff} is the effective energy barrier for the magnetization reversal. In addition, C and n are parameters of the Raman process, and τ_{QTM}^{-1} is the rate of the QTM process.[38] The parameters derived from the fit of the data to eqn (1) are shown in the insets of Fig. 7.

As shown in Fig. 7, the non-linear shape of the Arrhenius plots further corroborates the significant contribution of Raman and (possibly) QTM processes to the magnetization dynamics as the temperature is lowered. Specifically, at the intermediate and low-T regime, the relaxation time appears to be dominated by the Raman process as illustrated by the curvature of the ln τ *vs.* T^{-1} plots (Fig. 7) denoted by a power-law dependence (second term in eqn (1)).[39] In the high-T regime,

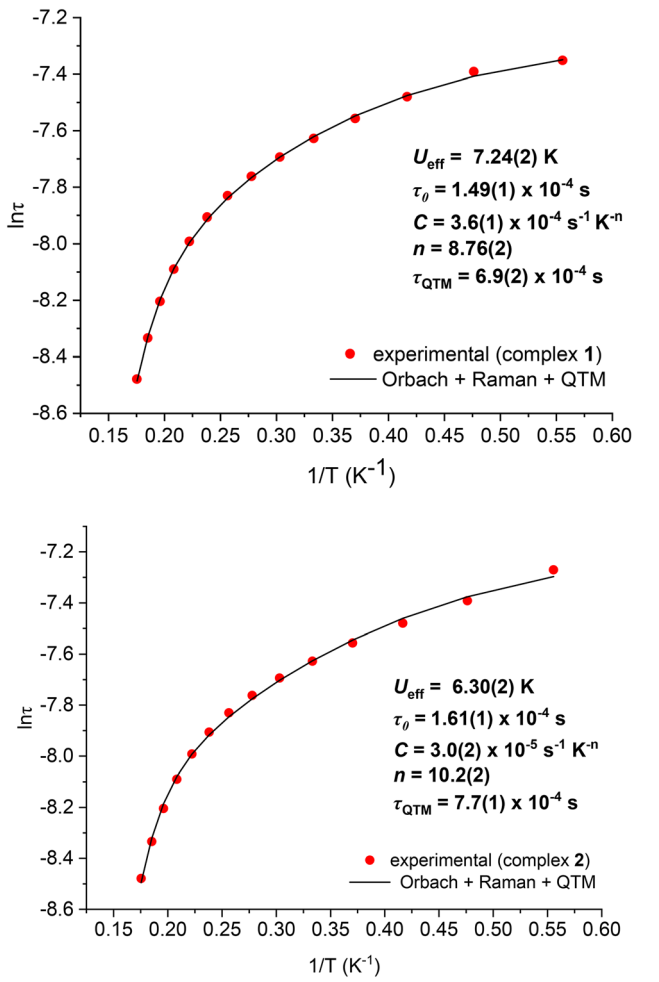

Fig. 7 Temperature dependence of the relaxation times (τ) according to the Arrhenius plot for **1** (top) and **2** (bottom) under zero applied dc field. The red circles correspond to experimental data and the black line is the best-fit of the data to eqn (1); see the insets for the fit parameters.

the thermally assisted Orbach process dominates and the relaxation time has an exponential dependence on temperature (linear region), giving similar U_{eff} values of 7.24(2) K (**1**) and 6.30(2) K (**2**) as well as τ_0 values of $1.49(1) \times 10^{-4}$ s (**1**) and $1.61(1) \times 10^{-4}$ s (**2**). The best-fit parameters, C and n, of the Raman process (inset of Fig. 7) are within the expected range for Dy^{III} SMMs.[9,10,38] In summary, the different coordination environments of the Dy^{III} centers in complexes **1** and **2** (muffin *vs.* tetradecahedral, respectively), do not appear to significantly affect the relaxation dynamics of the resultant complexes.

Complex **3** does not show any out-of-phase (χ''_M) signals at zero applied dc field; however, from the field dependence of the χ''_M *vs.* frequency (ν) plots at 2 K (Fig. S15†), an optimum dc field of 2000 Oe was extracted, and this was used to carry out detailed ac studies. At this field, complex **3** shows frequency- and temperature-dependent χ''_M signals in the temperature range of 1.8–4.6 K (Fig. 8), indicative of the slow magnetization relaxation of an SMM. The shapes of the Cole–Cole plots deviate significantly from the ideal semicircles (Fig. S16†), indicating the coexistence of thermally assisted and through barrier relaxation processes. This is further supported by the derived α values, which span the range 0.35–0.16 (Table S10†), reflecting a wide distribution of relaxation times and, *a fortiori*, the presence of multiple relaxation processes. Although application of an external magnetic field is known to suppress or even eliminate the QTM mechanism[9,12,39] we fitted the experimental $\ln\tau$ *vs.* T^{-1} data (Fig. 9) over the entire temperature range using eqn (1), which includes the contribution from the tunneling process. A very good fit was obtained, and this gave us U_{eff} and τ_0 values of 13.64(1) K and 9.34(1) $\times 10^{-6}$ s, respectively (inset of Fig. 9). As in the cases of **1** and **2**, the curved shape of the $\ln\tau$ *vs.* T^{-1} plot for **3** also suggests the presence of Raman and QTM processes, which

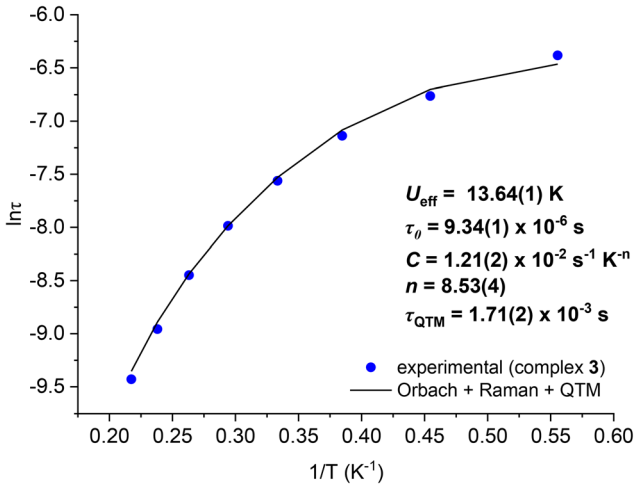

Fig. 9 Temperature dependence of the relaxation times (τ) according to the Arrhenius plot for **3** under a 2000 Oe applied dc field. The blue circles correspond to experimental data and the black line is the best-fit of the data to eqn (1); see the inset for the fit parameters.

turned out to be the case given the derived fitting parameters: $C = 1.21(2) \times 10^{-2}$ s^{-1} K^{-n}, $n = 8.53(4)$, and $\tau_{QTM} = 1.71(2) \times 10^{-3}$ s.

Complex **4**, the final member of this family of $\{Dy_2\}$ complexes and the only one that is nitrato-free, contains (as in **1** and **3**) nine-coordinate Dy^{III} atoms albeit in a spherical tricapped trigonal prismatic geometry. At zero external dc field, complex **4** exhibits tails of out-of-phase (χ''_M) signals at temperatures below 10 K (Fig. S17†), indicative of a fast relaxation process, which is predominantly driven by the QTM process. To slow down the relaxation process and force the magnetiza-

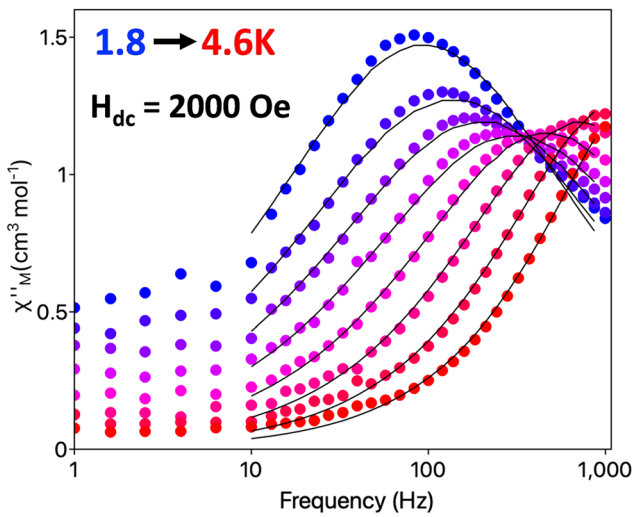

Fig. 8 Frequency-dependence of the out-of-phase (χ''_M) magnetic susceptibility data in an 2000 Oe dc field for **3**, measured at a 3.0 G ac field over the temperature range 1.8–4.6 K. Solid lines represent fits to the data, in the frequency range 10–1000 Hz, as described in the main text.

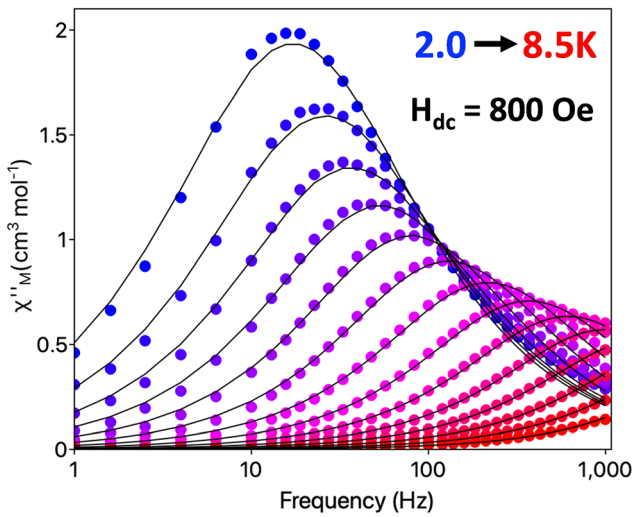

Fig. 10 Frequency-dependence of the out-of-phase (χ''_M) magnetic susceptibility data in an 800 Oe dc field for **4**, measured at 3.0 G ac field over the temperature range 2.0–8.5 K. Solid lines represent fits to the data, as described in the main text.

tion to thermally relax *via* the excited state(s), we applied an optimum dc field of 800 Oe determined from the fit of the χ''_M *vs.* frequency data at various fields (Fig. S18†). Indeed, under a small dc field of 800 Oe, fully visible out-of-phase signals, as a function of the ac frequency in the temperature range of 2.0–8.5 K, were observed for **4** (Fig. 10), which is characteristic of an SMM with an appreciable energy barrier for the magnetization reversal. A good fit of the temperature-dependent relaxation times, according to eqn (1), yielded a U_{eff} barrier of 69.62 (1) K and a τ_0 of $3.91(3) \times 10^{-5}$ s (Fig. 11), together with the corresponding parameters from the operating Raman and QTM processes (inset of Fig. 11). The α parameters resulting from the fit of the Cole–Cole plots (Fig. S19†), over the temperature range of 2.0–8.5 K, span the range 0.21–0.08, in agreement with a wide distribution of relaxation times.

The derived U_{eff} value of **4** is almost five times larger than that of **3** and an order of magnitude larger than those of **1** and **2**. This result is attributed to the Dy^{III} coordination environment in **4**, which likely induces a larger crystal field splitting of the ground $^6H_{15/2}$ state, as well as the exclusive presence of hynad$^-$ ligands, which foster a larger separation of the $\{Dy_2\}$ complexes which serves to minimize the transverse fields resulting from dipolar interactions between neighboring molecules, thereby reducing the efficiency of the tunneling relaxation. Retrospectively, the rare spherical tricapped trigonal prismatic polyhedron tends to have the capping vertices at the same distance from the center of the polyhedron.[40] This is the case for **4** (Fig. 4b); the distance of Dy1 to the three equatorial capping O donor atoms (O2′, O3 and O11), which belong to the neutral charged carbonyl O-atoms of hynad$^-$ and H_2O ligands, are 2.509(6), 2.522(7) and 2.429(7) Å, respectively. The two axial triangular faces of the prism contain the atoms O4/O5/O8 and O1/O1′/O7, most of which belong to the deprotonated O-donor atoms of the hynad$^-$ ligands. The bond distances between these atoms and the central Dy1 atom are much shorter (2.309(7)–2.447(6) Å) than those of the equatorial capping atoms. Thus, the anionic O-donors of the hynad$^-$ ligands are much closer to the Dy^{III} ions than the three equatorial ligands, and they will thus dominate the electronic structure. In turn, this will induce a relatively strong and axial crystal field above and below the Dy^{III} metal ions, which would enhance the oblate nature of the electron density of Dy^{III} in its electronic ground state, which explains the experimentally observed anisotropy barrier.[41]

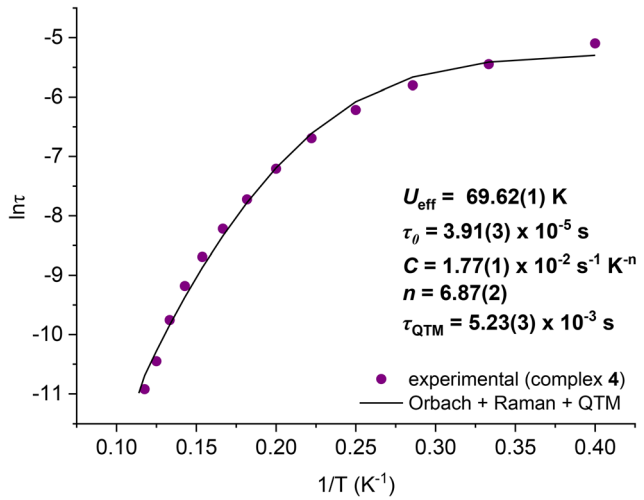

Fig. 11 Temperature dependence of the relaxation times (τ) according to the Arrhenius plot for **4** under an 800 Oe applied dc field. The purple circles correspond to experimental data and the black line is the best-fit of the data to eqn (1); see the inset for the fit parameters.

As a final comparison, all the pertinent features of compounds **1–4** with respect to their structural, and static and dynamic magnetic properties are compared in Table 1. In addition to the aforementioned impact of the Dy^{III} coordination geometry on the magnetic dynamics of **4**, only some tentative conclusions can be further derived by examining the information in Table 1, and these are restricted to a comparison between **1** and **3**, both of which contain 9-coordinate Dy^{III} atoms with muffin-like geometries. Following the conclusions extracted by the work of Tang and coworkers on complexes bearing the $\{Dy_2(\mu\text{-}OR)_2\}^{4+}$ core with the same coordination geometries, albeit with distinctly different Dy–O–Dy angles,[42] we mainly attribute the ferromagnetic response of **1** (*versus* the antiferromagnetic behavior of **3**) to the closer intramolecular Dy⋯Dy separations, the shorter Dy–O core distances, and the planarity of the bridging hynad$^-$ ligands with respect to the $\{Dy_2O_2\}$ core, provided that the Dy–O–Dy angles in **1** and **3** are essentially the same. To further reach a level of understanding on the differences between the obtained magnetic dynamics of **1** and **3**, we analyzed the muffin-like geometries of the corres-

Table 1 Selected structural and magnetic parameters for compounds **1–4**

Complex	**1**	**2**	**3**	**4**
Intramolecular Dy⋯Dy (Å) distance	4.018(4)	4.130(3)	4.094(3)	4.133(5)
Intermolecular Dy⋯Dy (Å) distance	7.209(4)	8.739(3)	10.885(3)	11.013(5)
Dy^{III} coord. number/geometry	9/muffin	10/tetradecahedron	9/muffin	9/spherical tricapped trigonal prism
Dy–O core distances (Å)	2.331(2)	2.377(2)	2.361(4)	2.384(6)
	2.332(3)	2.364(2)	2.417(4)	2.447(6)
Dy–O–Dy angle (°)	119.0(1)	121.2(1)	117.9(2)	117.6(2)
Distortion of hynad$^-$ over the $\{Dy_2O_2\}$ core (°)	5.4	13.0	14.7	28.6
Predominant magnetic exchange interactions	Ferromagnetic	Ferromagnetic	Antiferromagnetic	Ferromagnetic
U_{eff} (K)	7.24(2) (0 dc)	6.30(2) (0 dc)	13.64(1) (dc = 2000 Oe)	69.62(1) (dc = 800 Oe)

ponding Dy^{III} atoms (Fig. 1b and 3b).[43] To this end, in **1**, the equatorial pentagonal plane, which encompasses the oblate Dy^{III} center, is made of O1, O2, O4, O5, and O8 atoms, while the basal trigonal plane and the single atom vertex of the muffin, which are located below and above the DyO_5 plane, are formed by O6, O8′, O10′, and O9 atoms, respectively.[44] Interestingly, the stronger Dy–O bonds within the muffin topology are distributed among the atoms occupying both the equatorial pentagon [Dy1–O1 = 2.286(2) and Dy1–O8 = 2.331 (2)] and the axial triangular [Dy1–O8′ = 2.332(3)] subunits, likely causing a disorientation of the magnetic anisotropy from the pure axiality which explains the small U_{eff} value of **1**. In contrast to **1**, in complex **3**, the stronger Dy–O bond belongs to the single atom vertex [Dy1–O5 = 2.332(4)] of the muffin-like polyhedron, which could direct the projection of the magnetic anisotropy towards the axiality and away from the transverse crystal field, thus yielding a larger U_{eff} value (*vide supra*).

4. Conclusions

It has been demonstrated in this work that *N*-hydroxy-1,8-naphthalimide (hynadH) chelate facilitates the exclusive formation of dinuclear Dy^{III} complexes possessing a planar, diamond-shaped $\{Dy_2(\mu\text{-}OR)_2\}^{4+}$ core. The stable core can be modulated through the exchange of peripheral NO_3^- and $hynad^-$ groups, eventually leading to a family of four structurally-related compounds, $[Dy_2(hynad)_2(NO_3)_4(DMF)_2]$ (**1**), $(Me_4N)_2[Dy_2(hynad)_2(NO_3)_6]$ (**2**), $[Dy_2(hynad)_4(NO_3)_2(H_2O)_2]$ (**3**), and $[Dy_2(hynad)_6(H_2O)_2]$ (**4**). Compounds **1**, **2**, and **4** exhibit ferromagnetic coupling, whereas antiferromagnetic interactions appear to dominate in **3**. These observations are ascribed to the dissimilar structural and metrical features in **1–4**, including the Dy⋯Dy separations, Dy–O distances, and the degree of ligand distortion with respect to the $\{Dy_2O_2\}$ core. Furthermore, **1–4** exhibit slow relaxation of their magnetization at low temperatures, either in the absence (**1** and **2**) or presence (**3** and **4**) of an external dc magnetic field; as a result, they all behave as SMMs. The differences in the energy barriers for the magnetization reversal have been rationalized by means of comparing the individual Dy^{III} coordination polyhedra within **1–4**, and the possible orientations of the axial anisotropy axes with respect to the presence of stronger intramolecular Dy–O bonds.

Current efforts are directed at seeking new synthetic methods for retaining the $\{Dy_2(hynad)_2\}^{4+}$ core while introducing strongly bound alkoxides, phenoxides, or siloxides at the apical positions of the Dy^{III} coordination sites as a means of increasing the crystal field strength at the axial positions and therefore enhancing the easy-axis magnetic anisotropy and the energy barriers for the magnetization reversal. Given the stereochemical conformation of the ligand $hynad^-$ and its coordinating flexibility about the Dy^{III} atoms observed in **1–4**, it is reasonable to expect that upon additional chemical variations and synthetic modification, this chelate ligand will yield 4f-compounds of different nuclearities and topologies. The results of these studies will be reported in due course.

Conflicts of interest

The authors declare no competing financial interest.

Acknowledgements

L. C.-S. acknowledges financial support from Portuguese National Funds (FCT/MCTES, Fundação para a Ciência e a Tecnologia and Ministério da Ciência, Tecnologia e Ensino Superior) through the strategic projects UIDB/50006/2020 (for LAQV/REQUIMTE). L. C.-S. also thanks FCT/MCTES for funding through the Individual Call to Scientific Employment Stimulus (Ref. CEECIND/00793/2018). The SQUID magnetometer was purchased with funds provided by the Texas A&M University Vice President of Research.

References

1 (*a*) N. Ishikawa, M. Sugita, T. Ishikawa, S. Koshihara and Y. Kaizu, *J. Am. Chem. Soc.*, 2003, **125**, 8694–8695; (*b*) R. Layfield and M. Murugesu, *Lanthanides and Actinides in Molecular Magnetism*, John-Wiley & Sons, 2015; (*c*) P. Zhang, L. Zhang, C. Wang, S. Xue, S.-Y. Lin and J. Tang, *J. Am. Chem. Soc.*, 2014, **136**, 4484–4487; (*d*) T. Pugh, N. F. Chilton and R. A. Layfield, *Angew. Chem., Int. Ed.*, 2016, **55**, 11082–11085.

2 F. Habib and M. Murugesu, *Chem. Soc. Rev.*, 2013, **42**, 3278–3288.

3 (*a*) C. Papatriantafyllopoulou, E. E. Moushi, G. Christou and A. J. Tasiopoulos, *Chem. Soc. Rev.*, 2016, **45**, 1597–1628; (*b*) G. A. Craig and M. Murrie, *Chem. Soc. Rev.*, 2015, **44**, 2135–2147; (*c*) J. M. Frost, K. L. M. Harriman and M. Murugesu, *Chem. Sci.*, 2016, **7**, 2470–2491.

4 (*a*) D. Gatteschi, R. Sessoli and J. Villain, *Molecular Nanomagnets*, Oxford University Press, Oxford, 2006; (*b*) L. Sorace, C. Benelli and D. Gatteschi, *Chem. Soc. Rev.*, 2011, **40**, 3092–3104; (*c*) R. Sessoli and A. K. Powell, *Coord. Chem. Rev.*, 2009, **253**, 2328–2341.

5 (*a*) S. Kyatskaya, J. R. Galan-Mascarós, L. Bogani, F. Hennrich, M. Kappes, W. Wernsdorfer and M. Ruben, *J. Am. Chem. Soc.*, 2009, **131**, 15143–15151; (*b*) M. Urdampilleta, S. Klyatskaya, J.-P. Cleuziou, M. Ruben and W. Wernsdorfer, *Nat. Mater.*, 2011, **10**, 502–506.

6 L. Bogani and W. Wernsdorfer, *Nat. Mater.*, 2008, **7**, 179–186.

7 (*a*) R. Vincent, S. Klyatskaya, M. Ruben, W. Wernsdorfer and F. Balestro, *Nature*, 2012, **488**, 357–360; (*b*) M. Atzori and R. Sessoli, *J. Am. Chem. Soc.*, 2019, **141**, 1339–11352.

8 P. Konieczny, W. Sas, D. Czernia, A. Pacanowska, M. Fitta and R. Pełka, *Dalton Trans.*, 2022, **51**, 12762–12780.

9 (*a*) J. Tang and P. Zhang, *Lanthanide Single Molecule Magnets*, Springer, Berlin, Heidelberg, 2015; (*b*) Z. Zhu and J. Tang, *Natl. Sci. Rev.*, 2022, **9**, nwac194.
10 T. G. Ashebr, H. Li, X. Ying, X.-L. Li, C. Zhao, S. Liu and J. Tang, *ACS Mater. Lett.*, 2022, **4**, 307–319.
11 (*a*) J. D. Rinehart and J. R. Long, *Chem. Sci.*, 2011, **2**, 2078–2085; (*b*) V. S. Parmar, D. P. Mills and R. E. P. Winpenny, *Chem. – Eur. J.*, 2021, **27**, 7625–7645; (*c*) Y. Gil, A. Castro-Alvarez, P. Fuentealba, E. Spodine and D. Aravena, *Chem. – Eur. J.*, 2022, **28**, e20220033.
12 (*a*) J.-L. Liu, Y.-C. Chen and M.-L. Tong, *Chem. Soc. Rev.*, 2018, **47**, 2431–2453; (*b*) S. Bala, G.-Z. Huang, Z.-Y. Ruan, S.-G. Wu, Y. Liu, L.-F. Wang, J.-L. Liu and M.-L. Tong, *Chem. Commun.*, 2019, **55**, 9939–9942; (*c*) J. Liu, Y.-C. Chen, J.-L. Liu, V. Vieru, L. Ungur, J.-H. Jia, L. F. Chibotaru, Y. Lan, W. Wernsdorfer, S. Gao, X.-M. Chen and M.-L. Tong, *J. Am. Chem. Soc.*, 2016, **138**, 5441–5450; (*d*) Y.-S. Ding, N. F. Chilton, R. E. P. Winpenny and Y.-Z. Zheng, *Angew. Chem., Int. Ed.*, 2016, **55**, 16071–16074; (*e*) Y.-C. Chen, J.-L. Liu, L. Ungur, J. Liu, Q.-W. Li, L.-F. Wang, Z.-P. Ni, L. F. Chibotaru, X.-M. Chen and M.-L. Tong, *J. Am. Chem. Soc.*, 2016, **138**, 2829–2837; (*f*) A. B. Canaj, S. Dey, C. Wilson, O. Céspedes, G. Rajaraman and M. Murrie, *Chem. Commun.*, 2020, **56**, 12037–12040; (*g*) A. B. Canaj, S. Dey, E. R. Martí, C. Wilson, G. Rajaraman and M. Murrie, *Angew. Chem., Int. Ed.*, 2019, **58**, 14146; (*h*) Z. Li, Y. Zhai, W. Chen, Y. Ding and Y. Zheng, *Chem. – Eur. J.*, 2019, **25**, 16219–16224; (*i*) Z. Zhu, C. Zhao, T. Feng, X. Liu, X. Ying, X.-L. Li, Y.-Q. Zhang and J. Tang, *J. Am. Chem. Soc.*, 2021, **143**, 10077–10082.
13 (*a*) J. C. Vanjak, B. O. Wilkins, V. Vieru, N. S. Bhuvanesh, J. H. Reibenspies, C. D. Martin, L. F. Chibotaru and M. A. Nippe, *J. Am. Chem. Soc.*, 2022, **144**, 17743–17747; (*b*) J. P. Durrant, B. M. Day, J. Tang, A. Mansikkamäki and R. A. Layfield, *Angew. Chem., Int. Ed.*, 2022, **61**, e202200525; (*c*) F.-S. Guo, B. M. Day, Y.-C. Chen, M.-L. Tong, A. Mansikkamäki and R. A. Layfield, *Science*, 2018, **362**, 1400–1403.
14 (*a*) R. J. Blagg, L. Ungur, F. Tuna, J. Speak, P. Comar, D. Collison, W. Wernsdorfer, E. J. L. McInnes, L. F. Chibotaru and R. E. P. Winpenny, *Nat. Chem.*, 2013, **5**, 673–678; (*b*) A. Castro-Alvarez, Y. Gil, L. Llanos and D. Aravena, *Inorg. Chem. Front.*, 2020, **7**, 2478–2486.
15 F. Ortu, D. Reta, Y.-S. Ding, C. A. P. Goodwin, M. P. Gregson, E. J. L. McInnes, R. E. P. Winpenny, Y.-Z. Zheng, S. T. Liddle, D. P. Mills and N. F. Chilton, *Dalton Trans.*, 2019, **48**, 8541–8545.
16 (*a*) J. D. Rinehart, M. Fang, W. J. Evans and J. R. Long, *Nat. Chem.*, 2011, **3**, 538–542; (*b*) S. Demir, I.-R. Jeon, J. R. Long and T. D. Harris, *Coord. Chem. Rev.*, 2015, **289–290**, 149–176; (*c*) B. S. Dolinar, S. Gomez-Coca, D. I. Alexandropoulos and K. R. Dunbar, *Chem. Commun.*, 2017, **53**, 2283–2286; (*d*) B. S. Dolinar, D. I. Alexandropoulos, K. R. Vignesh, T. A. James and K. R. Dunbar, *J. Am. Chem. Soc.*, 2018, **140**, 908–911.
17 (*a*) C. A. Gould, K. R. McClain, D. Reta, J. G. C. Kragskow, D. A. Marchiori, E.-S. Choi, J. G. Analytis, R. D. Britt, N. F. Chilton, B. G. Harvey and J. R. Long, *Science*, 2022, **375**, 198–202; (*b*) Z. Zhu and J. Tang, *Chem. Soc. Rev.*, 2022, **51**, 9469–9481.
18 Y.-C. Chen and M.-L. Tong, *Chem. Sci.*, 2022, **13**, 8716–8726.
19 L. Palatinus and G. Chapuis, *J. Appl. Crystallogr.*, 2007, **40**, 786–790.
20 G. M. Sheldrick, *Acta Crystallogr., Sect. C: Struct. Chem.*, 2015, **71**, 3–8.
21 O. V. Dolomanov, L. J. Bourhis, R. J. Gildea, J. A. K. Howard and H. Puschmann, *J. Appl. Crystallogr.*, 2009, **42**, 339–341.
22 T. Kottke and D. Stalke, *J. Appl. Crystallogr.*, 1993, **26**, 615–619.
23 *APEX2 Data Collection Software Version 2.1-RC13*, Bruker AXS, Delft, The Netherlands, 2006.
24 *Cryopad Remote monitoring and control, Version 1.451*, Oxford Cryosystems, Oxford, United Kingdom, 2006.
25 *SAINT+ Data Integration Engine v. 7.23a © 1997–2005*, Bruker AXS.
26 G. M. Sheldrick, *SADABS v.2.01, Bruker/Siemens Area Detector Absorption Correction Program 1998*, Bruker AXS.
27 G. M. Sheldrick, *SHELXS-97, Program for Crystal Structure Solution*, University of Göttingen, 1997.
28 G. M. Sheldrick, *Acta Crystallogr., Sect. A: Found. Crystallogr.*, 2008, **64**, 112.
29 G. M. Sheldrick, *SHELXL-97, Program for Crystal Structure Refinement*, University of Göttingen, 1997.
30 (*a*) P. Van der Sluis and A. L. Spek, *Acta Crystallogr., Sect. A: Found. Crystallogr.*, 1990, **46**, 194–201; (*b*) A. L. Spek, *Acta Crystallogr., Sect. C: Cryst. Struct. Commun.*, 2015, **71**, 9–18.
31 K. Brandenburg, *DIAMOND, Release 3.1f*, Crystal Impact GbR, Bonn, Germany, 2008.
32 J. Bruno, J. C. Cole, P. R. Edgington, M. K. Kessler, C. F. Macrae, P. McCabe, J. Pearson and R. Taylor, *Acta Crystallogr., Sect. B: Struct. Sci.*, 2002, **58**, 389–397.
33 G. A. Bain and J. F. Berry, *J. Chem. Educ.*, 2008, **85**, 532–536.
34 C. Xia, S. Wu, Y. Liang, Z. Chen, H. Zou and F. Liang, *Transition Met. Chem.*, 2015, **40**, 839–846.
35 (*a*) Th. C. Stamatatos and E. Rentschler, *Chem. Commun.*, 2019, **55**, 11–26; (*b*) Z. G. Lada, C. D. Polyzou, V. Nika, Th. C. Stamatatos, K. F. Konidaris and S. P. Perlepes, *Inorg. Chim. Acta*, 2022, **539**, 120954.
36 M. Llunell, D. Casanova, J. Girera, P. Alemany and S. Alvarez, *SHAPE, version 2.0*, Universitat de Barcelona, Barcelona, Spain, 2010.
37 K. S. Cole and R. H. Cole, *J. Chem. Phys.*, 1941, **9**, 341–351.
38 (*a*) S. T. Liddle and J. van Slageren, *Chem. Soc. Rev.*, 2015, **44**, 6655–6669; (*b*) E. Garlatti, A. Chiesa, P. Bonfà, E. Macaluso, I. J. Onuorah, V. S. Parmar, Y.-S. Ding, Y.-Z. Zheng, M. J. Giansiracusa, D. Reta, E. Pavarini, T. Guidi, D. P. Mills, N. F. Chilton, R. E. P. Winpenny, P. Santini and S. Carretta, *J. Phys. Chem. Lett.*, 2021, **12**, 8826–8832; (*c*) R. Orbach, *Proc. R. Soc. London, Ser. A*, 1961, **264**, 1319.

39 (*a*) Y.-C. Chen, J.-L. Liu, W. Wernsdorfer, D. Liu, L. F. Chibotaru, X.-M. Chen and M.-L. Tong, *Angew. Chem., Int. Ed.*, 2017, **56**, 4996–5000; (*b*) M. Briganti, F. Santanni, L. Tesi, F. Totti, R. Sessoli and A. Lunghi, *J. Am. Chem. Soc.*, 2021, **143**, 13633–13645.

40 E. C. Mazarakioti, J. Regier, L. Cunha-Silva, W. Wernsdorfer, M. Pilkington, J. Tang and Th. C. Stamatatos, *Inorg. Chem.*, 2017, **56**, 3568–3578.

41 N. F. Chilton, D. Collison, E. J. L. McInnes, R. E. P. Winpenny and A. Soncini, *Nat. Commun.*, 2013, **4**, 1–7.

42 (*a*) L. Zou, L. Zhao, P. Chen, Y.-N. Guo, Y. Guo, Y.-H. Lib and J. Tang, *Dalton Trans.*, 2012, **41**, 2966–2971; (*b*) P. Zhang, L. Zhang, S.-Y. Lin, S. Xue and J. Tang, *Inorg. Chem.*, 2013, **52**, 4587–4592; (*c*) Y.-N. Guo, X.-H. Chen, S. Xue and J. Tang, *Inorg. Chem.*, 2011, **50**, 9705–9713.

43 A. S. Armenis, G. P. Bakali, C. L. Brantley, C. P. Raptopoulou, V. Psycharis, L. Cunha-Silva, G. Christou and Th. C. Stamatatos, *Dalton Trans.*, 2022, **51**, 18077–18089.

44 (*a*) P. Antal, B. Drahoš, R. Herchel and Z. Trávníček, *Dalton Trans.*, 2016, **45**, 15114–15121; (*b*) L. Mandal, S. Biswas and M. Yamashita, *Magnetochemistry*, 2019, **5**, 56.